

# Rupture processes of the 2013–2014 Minab earthquake sequence, Iran

Jonas A. Kintner,<sup>1</sup> Charles J. Ammon,<sup>1</sup> K. Michael Cleveland<sup>2</sup> and Matthew Herman<sup>1</sup>

<sup>1</sup>*Department of Geosciences, The Pennsylvania State University, University Park, PA 16802, USA. E-mail: jvk5803@psu.edu*

<sup>2</sup>*Los Alamos National Laboratory, Los Alamos, NM 87545, USA*

Accepted 2018 February 28. Received 2018 January 18; in original form 2017 October 2

## SUMMARY

We constrain epicentroid locations, magnitudes and depths of moderate-magnitude earthquakes in the 2013–2014 Minab sequence using surface-wave cross-correlations, surface-wave spectra and teleseismic body-wave modelling. We estimate precise relative locations of 54  $M_w \geq 3.8$  earthquakes using 48 409 teleseismic, intermediate-period Rayleigh and Love-wave cross-correlation measurements. To reduce significant regional biases in our relative locations, we shift the relative locations to align the  $M_w$  6.2 main-shock centroid to a location derived from an independent InSAR fault model. Our relocations suggest that the events lie along a roughly east–west trend that is consistent with the faulting geometry in the GCMT catalogue. The results support previous studies that suggest the sequence consists of left-lateral strain release, but better defines the main-shock fault length and shows that most of the  $M_w \geq 5.0$  aftershocks occurred on one or two similarly oriented structures. We also show that aftershock activity migrated westwards along strike, away from the main shock, suggesting that Coulomb stress transfer played a role in the fault failure. We estimate the magnitudes of the relocated events using surface-wave cross-correlation amplitudes and find good agreement with the GCMT moment magnitudes for the larger events and underestimation of small-event size by catalogue  $M_S$ . In addition to clarifying details of the Minab sequence, the results demonstrate that even in tectonically complex regions, relative relocation using teleseismic surface waves greatly improves the precision of relative earthquake epicentroid locations and can facilitate detailed tectonic analyses of remote earthquake sequences.

**Key words:** Earthquake source observations; Seismicity and tectonics; Surface waves and free oscillations.

## INTRODUCTION

On 2013 May 9, a sequence of moderate-size earthquakes initiated about 100 km southeast of the city of Minab in south-central Iran (Fig. 1). Two people were killed and 20 injured in the sparsely populated epicentral region (International Seismological Centre 2014). The largest event in the 2013 sequence, an  $M_w$  6.2 (GCMT) earthquake that occurred at 02:08:08.500 UTC on 2013 May 11, was preceded by four foreshocks and 70 aftershocks with estimated magnitudes above 3.5 occurred during the following year. The main-shock hypocentre was located at 26.560N, 57.770E with a fixed depth of 15 km;  $m_b$ ,  $M_S$  and  $M_w$  estimates are 5.9, 6.2 and 6.1 respectively (USGS). This sequence occurred in western Makran, an east–west striking subduction and accretionary structure forming the southeastern boundary of Iran and western Pakistan (Byrne *et al.* 1992). GPS studies of the region indicate that the Arabian and Eurasian convergence rate is  $\sim 2$ – $4$  cm yr<sup>-1</sup> (Vernant *et al.* 2004; Smith *et al.* 2012; Frohling & Szeliga 2016), with Arabia moving in a north–northeast direction. According to the ISC catalogue, this region of this accretionary prism appears to have experienced moderate-magnitude seismic

events every 10–15 yr since at least the mid-1930s (Supporting Information Fig. S6).

The 2013 sequence was located about 125 km north of the coastline and about 250–300 km north of the western segment of the Makran Subduction Zone Deformation Front. Previously computed moment tensor solutions, slip distributions estimated using InSAR data and field observations (GCMT catalogue; Samsonov & Czarnogorska 2013; Penney *et al.* 2015) suggest that the main shock occurred on near-vertical, left-lateral strike-slip structures, oriented almost perpendicular to the nearby Minab–Zendan–Palami (MZP) fault, the largest regional structure observed at the surface. Receiver-function analysis and tomographic investigations suggest that the subducting Arabian plate is continuous and deepens from west to east at the transition between continental collision and subduction (Yamini-Fard *et al.* 2007, Yamini-Fard & Harzfeld 2008). Penney *et al.* (2015) suggested that this continuous coupling causes shearing within the upper plate due to the traction on the plate interface. Left-lateral strike-slip faulting in western Makran is thought to reactivate reverse faults associated with deformation related to plate convergence (Penney *et al.* 2017).

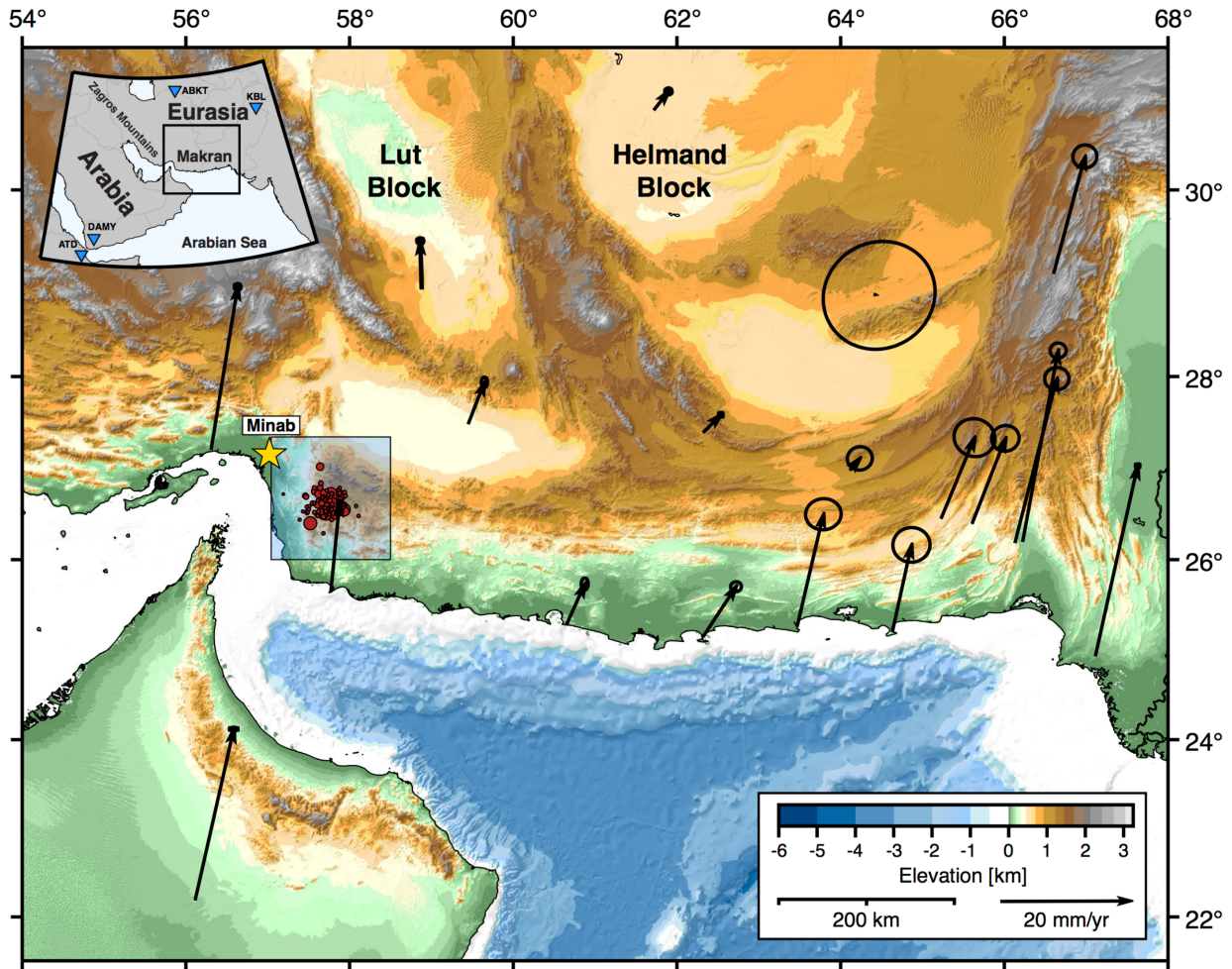


**Figure 1.** Regional map of the Makran area. The inset on the top left shows the Makran region relative to the Middle East and parts of Eurasia, blue inverted triangles show the locations of nearby teleseismic stations. The arrows show the regional GPS velocities relative to Eurasia from Frohling & Szeliga (2016). The seismicity from the Minab Sequence is shown in the blue boxed region in western Makran. The earthquakes from the Minab Sequence are marked as red circles, the locations are NEIC epicentres  $M > 3.5$  from 2013 to 2015, scaled to NEIC magnitude. The city of Minab lies northwest of the seismicity, its location is marked with a gold star.

We have two goals. The first is to provide additional insight on the 2013–2014 Minab earthquake sequence. Contributing precise locations for the events in this sequence permits a better understanding of the faulting that occurred and some insight into deformation within Makran’s accretionary wedge material. The region surrounding Minab has not recently hosted any large events—the 2013 event is one of the largest in the ISC catalogue. Comparable-size events occurred in 1933 ( $M_S$  5.6), 1947 ( $M_S$  6.2), 1962 ( $M$  5.5), 1969 ( $m_b$  5.2) and 1983 ( $M_S$  5.7) (Supporting Information Fig. S6). The Minab sequence was not unique, but neither was it typical. The sequence began with a few foreshocks, one with  $M_w$  5.0. The  $M_w$  6.2 main shock was followed by aftershocks that have a cumulative moment that is roughly 60 per cent of the main-shock moment (GCMT catalogue). As shown below, the largest of these aftershocks are associated with a westward migration of deformation in the days following the main shock. Our second goal is to illustrate the value of multiple-event relocation using teleseismic surface-wave observations in remote and potential complex continental regions. The method has been applied to events along oceanic transform faults (Cleveland & Ammon 2013; Cleveland *et al.* 2015), an environment with a relatively uniform intermediate-period dispersion, faulting geometry and centroid depth. The Minab sequence includes events

with similar faulting geometry (and depth, as shown below), and we show that the dispersion expected for a continental region is not a substantial hurdle in the relative relocation of nearby (several tens of kilometres) events, even when we extend the analysis to shorter periods and smaller-magnitude earthquakes.

## EARTHQUAKE RELOCATIONS FOR THE MINAB SEQUENCE

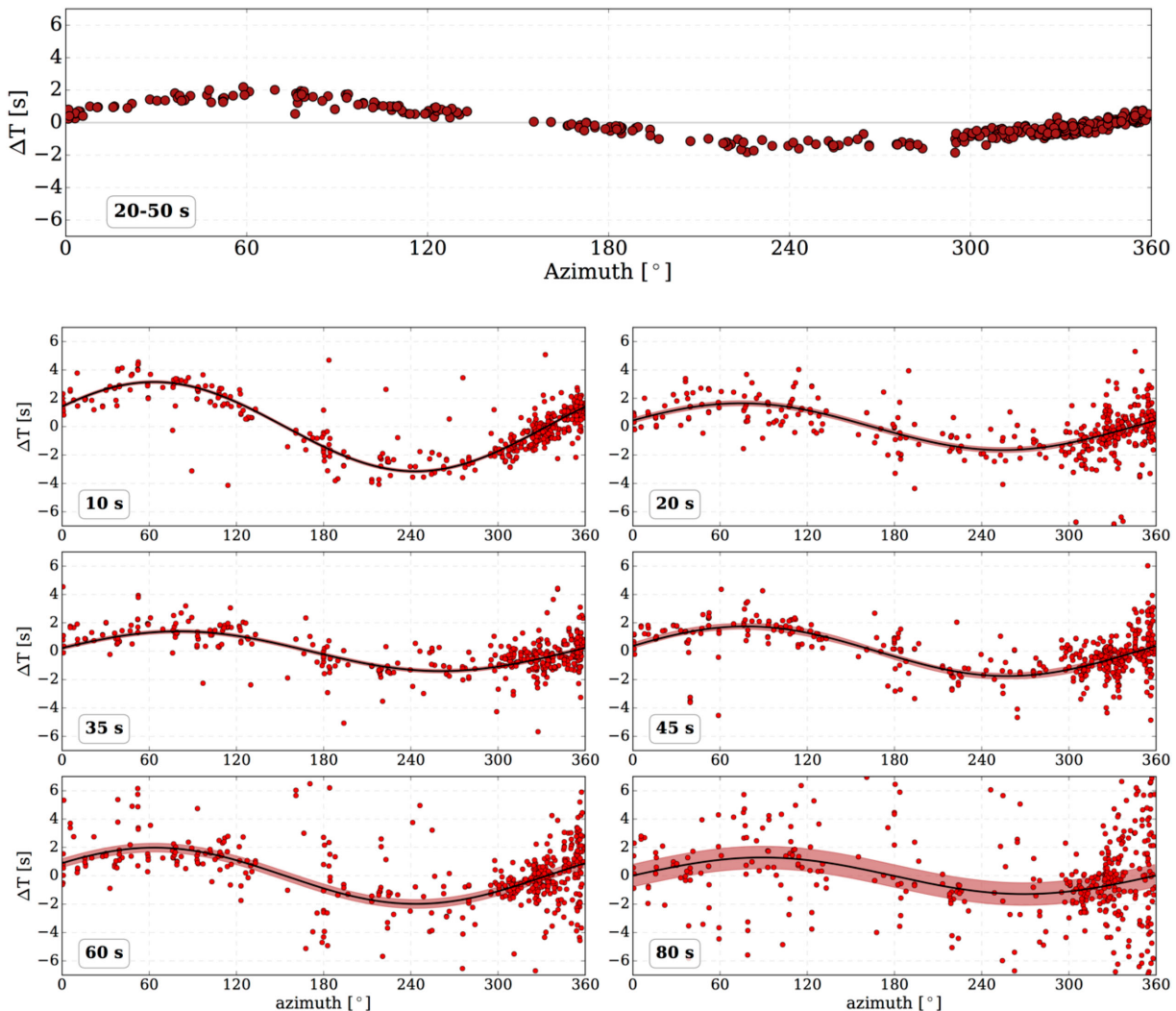
We use the surface-wave based centroid relocation method developed by Cleveland & Ammon (2013) and Cleveland *et al.* (2015). The method employs differential arrival times of surface waves measured using cross-correlation of intermediate-period signals. The relative slow propagation speed of surface waves allows relatively precise location estimates for shallow earthquakes, which are also well observed at teleseismic distances. Cleveland & Ammon (2013) and Cleveland *et al.* (2015) assumed that the events are similar in faulting geometry, and occur in a region with little variation in intermediate period surface-wave slowness. For a first-order oceanic velocity structure, surface-wave group slowness in the 30–80 s band is relatively uniform. In this study, we apply the method to a set of moderate and smaller-magnitude events in a region with a more

complex crustal velocity that includes relatively slow near-surface material. To accommodate for the smaller-magnitude events, we shift the bandwidth to include the more dispersive shorter period signals, but for small inter-event distances involved here, this does not cause problems.

We began with a list of USGS-NEIC hypocentres for events that occurred between 2013 January 1 and 2015 January 1 in the region defined by latitude 25.5–27.4N and longitude 56.8–59.4E. Long-period (one sample per second) seismograms were acquired from the IRIS data centre for all stations operating during the event times. Displacement waveforms were computed using a frequency-domain instrument response deconvolution, and signals were visually inspected for quality control purposes and assigned a grade (A, B, C, D, F) based on signal clarity. Only C quality or better are used for the relocation. The waveforms were group-velocity windowed between 2 and 5 km s<sup>-1</sup>, then filtered with a zero-phase Butterworth bandpass filter (period ranges discussed below). Cross-correlations were computed for each station and all available event-pair combinations. The maximum cross-correlation lag and amplitudes are recorded and used in subsequent event relocation and relative

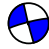








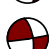
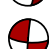
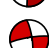
magnitude inversions. A single event-pair cross-correlation data set (all stations) is shown at the top of Fig. 2. The full bandwidth time-domain observations (top panel) are dense and consistent.

The relocation algorithm is a least-squares implementation of a double-difference approach originally described in Waldhauser & Ellsworth (2000), but applied to a sphere. Depth is not included, but is analysed using body waveforms and spectra (discussed later). For specific method details, we refer the reader to Cleveland & Ammon (2013). We performed the earthquake relocations in two steps. We began relocating the larger events within the Minab sequence—those with GCMT solutions (Table 1). We used average Rayleigh and Love wave group slowness for the period range between 30 and 80 s periods computed using the velocity model from Yamini-Fard *et al.* (2007) (corresponding group speeds were  $\sim 3.54$  and 3.77 km s<sup>-1</sup> for Rayleigh and Love waves respectively). Given the large number of observations available for moderate-magnitude observations, we applied the relatively stringent minimum acceptable normalized cross-correlation value (0.90) used by earlier studies (Cleveland & Ammon 2013; Cleveland *et al.* 2015). The minimum number of observations for two events to link was set to 4. The



**Figure 2.** Cross-correlation phase differences between the Rayleigh waves of event pair 05/11/2013 02:08:08 and 05/18/2013 10:03:16. The top panel shows the traveltime differences as a function of azimuth for waveforms bandpass filtered between 20 and 50 s, the band used in the relative relocation. The bottom six panels show the cross-correlation phase with azimuth at different periods, scaled by period/ $2\pi$ . Red shading shows the 2-sigma uncertainties of the iteratively reweighted sinusoidal pattern fit. Period in seconds is listed at the bottom left corner of each panel.

**Table 1.** Relocation results. Event index and mechanism colour are chronological in time to match Figs 3 and 4. Mechanisms are from the GCMT catalogue; red circle indicates that there is no GCMT solution. Latitude and longitude are the relocation results. Italicized depths are poorly constrained or from original NEIC catalogue, non-italic are the estimated depths and relative magnitudes from this study.

Index		Origin Time	Latitude (deg)	Longitude (deg)	Depth (km)	Magnitude ( $M_w$ )
1		05/09/2013 08:01:34	26.665	57.881	<i>20.3</i>	5.10
2		05/11/2013 02:08:08	26.675	57.916	6.1	6.28
3		05/11/2013 03:09:47	26.703	57.963	<i>12.2</i>	5.54
4		05/11/2013 03:41:27	26.705	57.927	<i>10.0</i>	5.19
5		05/11/2013 08:42:36	26.668	57.919	<i>23.1</i>	4.94
6		05/11/2013 18:06:13	26.685	57.917	25	4.78
7		05/12/2013 00:06:59	26.663	57.891	8.5	5.62
8		05/12/2013 10:54:48	26.661	57.882	8.2	5.59
9		05/18/2013 10:03:16	26.660	57.859	5.1	5.61
10		05/18/2013 10:57:47	26.657	57.862	7.0	5.56
11		05/20/2013 09:16:30	26.665	57.816	<i>24.2</i>	4.69
12		02/02/2014 14:26:45	26.659	57.831	<i>7.0</i>	5.36

minimal linking criterion allows for more events to be included in the inversion, but we identify minimally linked events as low quality in the table of relocations (Supporting Information Table S1). Events with the highest quality require a minimum of 12 links between all event pairs, as suggested in Cleveland & Ammon (2013). The maximum linking distance (100 km) is roughly the dimension of our shortest wavelength and large enough to include all events in the sequence.

With no ground-truth information, a relatively relocated cluster of events can be shifted in space without changing the misfit, as long as individual events are not shifted in reference to one another. The Minab sequence exhibited little surface faulting, but did produce InSAR signals (that have been modelled by Penney *et al.* 2015). We therefore constrained the main-shock epicentroid location to be consistent with the estimate from InSAR (Penney *et al.* 2015). InSAR data can be used to determine the rupture zone of shallow earthquakes (e.g. Engdahl *et al.* 2007), and its use as a tool for removing systematic regional biases in event location has been suggested for a number of events in the region (e.g. Lohman & Simons 2005). An error in our constrained main-shock centroid location directly affects our absolute, but not our relative locations.

Following the initial relocation of the moderate-magnitude events with GCMT solutions, we included the remaining events from the NEIC catalogue—a total of 80 earthquakes that occurred between 2013 January 1 and 2015 January 1 with NEIC magnitudes ranging between  $m_b$  3.8 and  $M_w$  6.1 were available. To improve the signal quality and quantity for the smaller events, we modified the analysis bandwidth to 20–50 s, and lowered the normalized cross-correlation threshold to 0.80. The bandwidth shift from 30–80 to 20–50 s necessitates a slowness increase (corresponding to average group speed reduction to  $\sim 3.38$  and  $3.58$  km s<sup>-1</sup> for Rayleigh and Love waves respectively). The shift also moves the analysis towards the signal

band that often shows a strong dispersion resulting from the influence of crustal and mantle speed on signals. To include an event in the relocation, we must assume that the event has a faulting geometry and depth compatible with the larger events. For many of the smaller events, the cross-correlation patterns support the assumption. Events with non-systematic cross-correlation patterns were eliminated by the cross-correlation selection criteria, or produced low-quality relocations (and are identified as such in the results). Numerical experiments showed that our initial moderate-magnitude event locations were not negatively affected by these changes. To check the consistency and reliability of the measurements, we examined the cross-correlation phase shifts for indications of dispersive and noise artefacts in the frequency domain.

Fig. 2 is a summary of the Rayleigh wave time and frequency domain observations computed using the main shock (05/11/2013 02:08:08) and the 05/18/2013 10:03:16 aftershock (Table 1). The top panel of Fig. 2 is a plot of the time of the maximum amplitude in the 20–50 s band cross-correlation (i.e. the data used in our relocations). Despite the relatively small amplitude of the time-domain sinusoidal pattern, which indicates that the events are close, the azimuthal pattern is clear and strong. The bottom six panels show corresponding scaled cross-correlation phase values for periods ranging from 10 to 80 s. Each phase observation was scaled by the period divided by  $2\pi$  to ease comparison of the observations. Such a scaling maps each observation onto an equivalent time-shift range, which depends on the distance between the events and the slowness at that period. As expected, individual period phase measurements exhibit more scatter than the integrated time-domain measurements. The scatter is largest for the longest periods, because the time-shift associated with the difference in centroid location is a small fraction of the  $\sim 60$ –80 s periods and is hard to measure precisely. The solid lines and shaded regions show an iteratively

reweighted least-squares sinusoidal fit to the phase shifts and the associated uncertainty (uncertainties are scaled using the covariance matrix of the sinusoidal model parameters, then mapped to standard deviations in amplitude and phase, assuming a Gaussian distribution). Observations for each period produce a consistent pattern that mimics the time-domain average. To first order, each period produces a sinusoid with extrema at the same azimuths (aligned with the direction connecting the two event centroids).

For events with similar depth and focal mechanisms, the phase-shift sinusoid amplitudes are controlled by the interevent centroid distance and the phase slowness at the corresponding period. The fact that the phase-shift amplitudes are comparable for the period range from 20–50 s shows the slowness in this range is relatively well approximated with a uniform value, and the observations suggest that phase slownesses are consistent with the 1-D velocity model for the region. The exception is the phase shifts for a period of 10 s. The 10 s pattern in Fig. 2 shows a notably larger amplitude than those from periods in the range from 20–60 s. The inference is that the phase velocity changes significantly between 10 s and 20 s. Based on these observations, we limited our period range used in the locations to 20–50 s. That range appears consistent with the use of a single, mean slowness in the relocation, but provides a sufficient bandwidth to include smaller-magnitude aftershocks into the relocation. However, factors such as small event size, lack of good azimuthal coverage, and/or possible differences in focal mechanism or depth, only 54 events of the targeted 80 events (including the 12 with GCMT solutions) produce sufficient data to be relocated. The 54 events are discussed below, and all 80 events are listed in Supporting Information Table S1.

We estimated relative location uncertainties using the model covariance matrix scaled by the data variance (e.g. Menke 2012). We estimated the data variance using the average unweighted double-difference misfit (1.35 s). All formal two-standard deviation uncertainties in latitude and longitude are less than  $\pm 5.0$  km from each event epicentroid (Fig. 4). Formal uncertainties are larger for earthquakes with fewer high-quality cross-correlation observations in the aftershock sequence (possibly because of differences in faulting orientation or depth relative to the rest of the sequence). The formal relative location uncertainties are minimal in that they do not include uncertainties associated with earth structure or differences in faulting geometry and depth that could affect the signal phase. We directly explored the sensitivity of the locations to the assumed average surface-wave slowness. The sensitivity tests suggest that the entire distribution of events can be expanded or contracted by a few kilometres, shifting individual event locations by  $\sim 1$ –2 km. More realistic relative epicentroid uncertainty estimates are  $\sim 2$ –3 km for most of the larger events in this sequence. Assessing focal mechanism effects is more difficult. Cleveland & Ammon (2013) suggest that small to moderate perturbations in depth and focal mechanism do not significantly affect relative location accuracy. In this study, we make the initial assumption that a majority of the smaller events have similarities in faulting geometry and depth. We are sure that including these smaller events did not affect the locations estimated using only events for which the GCMT solutions confirm the faulting geometry similarity. Consistency in the spatial patterns of the relocations with each other and with independent GCMT faulting information provides confidence in the overall pattern of the event locations. Events that locate outside the main cluster of events are more difficult to confirm, most are small and have fewer observations than the well-constrained events that lie near the main shock. But these events represent a small fraction of the 54 relocations.

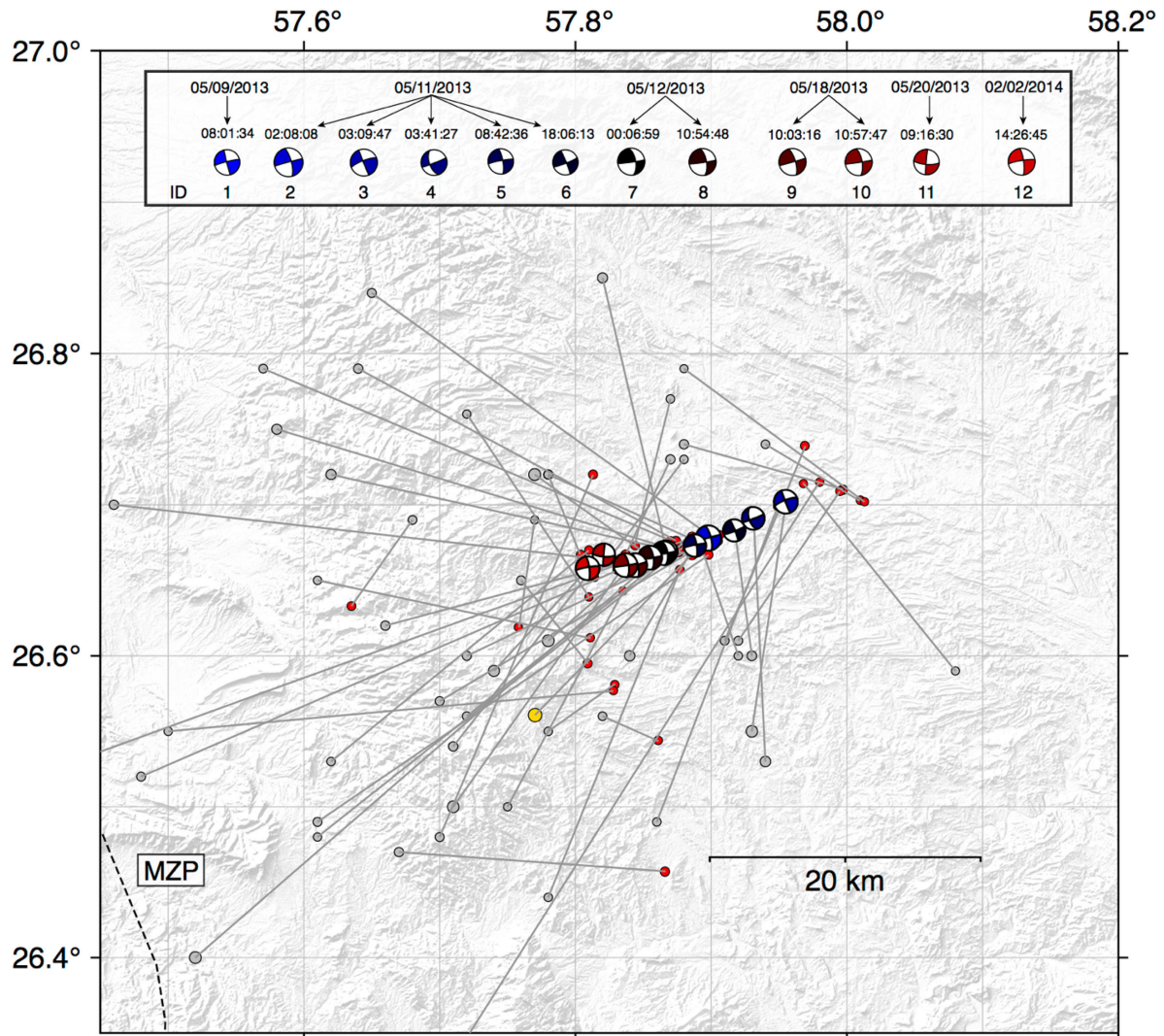
## RELOCATION RESULTS

Fig. 3 is a map showing the initial and final epicentre locations and Fig. 4 is a close up of the main cluster of events associated with the largest strain release. The initial NEIC locations (Figs 1, 3 and 5) are significantly scattered and hard to associate with any simple spatial pattern. Even the initial locations of the moderate-magnitude epicentres are diffuse. The same is true of the earthquake locations contained in the ISC and Tehran University, Institute of Geophysics (2016) catalogue (Fig. 5).

The full list of NEIC locations we examined is provided in Supporting Information Table S1. Each event is assigned a quality (zero for events with no confidence, one for events with modest confidence and two for events with substantial confidence). Quality-two events have 12 or more links in each event pairing; quality-one events have at least four links in each event pairing, quality-zero events were not relocated due to a lack of high quality observations. Twenty-six of the 80 events produced little to no consistent observations and are listed as quality-zero events. Ten of the 80 events are quality-one, these are events that were poorly constrained due to limited observations. Forty-four of the 80 events are quality-two, the best solutions with a large number of observations between individual event pairs and surrounding earthquakes. The original and final locations of events with a quality-one or better are shown in Fig. 3.

A statistical summary of the relocation results for all events with quality-one or better (Supporting Information Table S1) is presented in Supporting Information Fig. S4. The number of total observations used for each event ranged from 10 to almost 7400 double difference observations, with an average number of 1744 and median number of 733. The mean and median number of observations between individual event pairs are 49 and 16, respectively. Estimated event time-shifts range from  $-7$  to 15 s (quality-two events have a range between  $-5$  and 5 s). The large 4.97 s origin time-shift seen in the main shock includes differences between the origin time (initial value) and the centroid time (what we estimate). The mean time-shift was 0.0 s, the median was  $-0.06$  s and the standard deviation was 3.0 s. The average spatial shift for the relocated events (including the shift from the InSAR constraint) was 19.3 km, the standard deviation was 12.1 km. The distances between NEIC, GCMT and ISC main-shock epicentre locations with the InSAR centroid location were 18.3, 21.9 and 5.8 km respectively. These values are generally consistent with Weston *et al.* (2011), who compares the epicentre locations of various global catalogues with the InSAR centroid locations of moderate magnitude events around the globe. The maximum shift of a GCMT event was 45.4 km and corresponds to the  $M_w$  5.6 event on 05/12/2013 00:06:59 that lies near the MZP fault system (Fig. 3). The overall variance reduction in the double-difference inversion was 83 per cent (initial absolute average misfit was 4.1 s and the final was 1.35 s).

The formal two-sigma uncertainties are shown in Fig. 4 using crosses. All relocated event formal uncertainties are less than 5 km. Despite smaller formal uncertainties, we speculate that the well-constrained event epicentroid locations are certain only to within a few kilometres since the formal uncertainties do not take into consideration that effects of earth structure, differences in mechanism, nor the possibility that the main-shock centroid of the InSAR solution may not be the true midpoint of the main-shock rupture. Our relocation pattern could reasonably be shifted at least several kilometres in either direction along the fault if future observations require it. Aftershocks with fewer and noisier observations have higher formal uncertainties and appear to be off axis from the main left lateral structure. Combined with the information in the GCMT



**Figure 3.** Event relocation results from this study (quality-one or better locations from Supporting Information Table S1). The main-shock centroid was fixed at 57.898E, 26.698N, the centre of the uniform slip model from Penney *et al.* (2015). Focal mechanisms and red circles show the final centroid locations calculated using surface waves. The focal mechanisms are coloured by time, the legend shows the origin time, mechanism and ID number from Table 1. Grey/yellow circles are the original locations (yellow is the original location of the  $M_w$  6.1 main shock). The dashed line is the Minab–Zendan–Palami (MZP) fault system.

solutions, the structure involved in the sequence is a left-lateral strike-slip fault with a total length of about 15–20 km. As a simple check on the large event locations, we compare the before and after alignment of  $SH$  waves recorded at station TAM (Tamanrasset, Algeria, 22.79N, 5.53E) in Supporting Information Fig. S3. The relocations show a more consistent alignment of these independent data and provide some confidence in the relocations, some of which shifted the events by up to  $\sim 45$  km. The majority of relocated epicentroids align along strike of what appears to be WSW striking structure with a handful of events that remain diffuse (many of which are identified as lower quality) surrounding the main cluster (Fig. 4). We postpone a detailed discussion of the relocations until the Discussion section.

### RELATIVE EARTHQUAKE MAGNITUDES

The cross-correlation measurements also carry information on relative event size. We use a multiple-event algorithm developed by

Cleveland & Ammon (2015), which extends the two-event approach of Schaff & Richards (2011, 2014) to estimate the logarithms of the relative seismic moment of events in the Minab sequence. A linearized inversion using the un-normalized cross-correlations for events with quality one and two was performed to estimate the logarithm of the moments of the earthquakes. A constraint is applied to provide an absolute reference. We require that the sum of the log-moments of the GCMT events match the sum of the log-moments of the corresponding events in Table 1. In other words, we require that our estimated moments for the larger events and the GCMT moments are compatible on average. We iteratively down-weighted observations with residuals larger than two standard deviations from the mean of the original residuals and performed a total of nine iterations. Formal uncertainties were computed in a similar manner to the uncertainties in location. The covariance matrix is scaled using an estimate of the data variance constructed using residuals from the least squares solution (Aster & Thurber 2013, and eq. 5 in Cleveland & Ammon 2015). The large number of cross-correlations (48 409) used to constrain 54 quantities results in small uncertainties

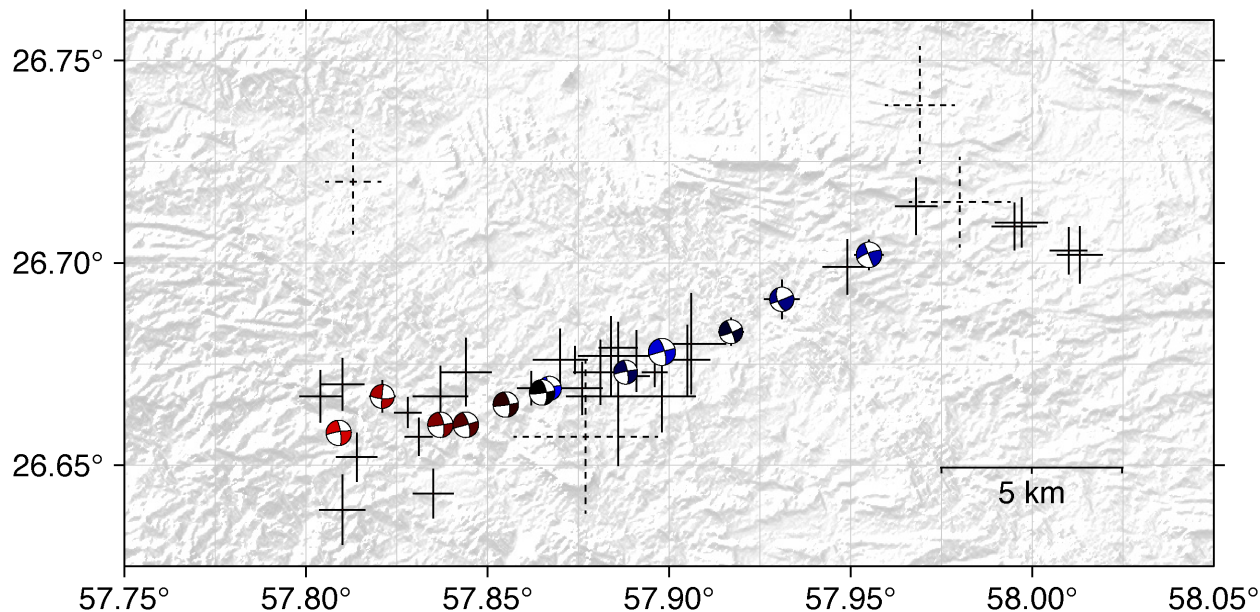


**Figure 4.** Two-standard-deviation error bars for the relocated events in this study (quality-one and quality-two events from Supporting Information Table S1). GCMT focal mechanisms are plotted on their respective final event locations, coloured by time from blue as earliest and red as latest (see Fig. 3). Dashed error bars identify events that we classify as lower quality. Formal uncertainties are computed through scaling the model covariance by a data variance (we used the final misfit in travel time differentials, 1.4 s, as the standard deviation).

for the magnitudes. All uncertainties are within  $\pm 0.01$  magnitude units. Such small uncertainties are statistically reasonable but beyond the precision needed for magnitude—they do not account for variations in the faulting geometry and depth, which increase the true uncertainty.

The relative magnitudes computed from this sequence are shown in Fig. 6. We compare our relative magnitudes to a selected preferred magnitude obtained from the ISC catalogue. We select a magnitude in the following order, from most to least preferred: GCMT- $M_w$ , NEIC- $M_w$ , NEIC- $M_S$ , ISC- $M_S$ , IDC- $M_S$ , NEIC- $m_b$ , NEIS- $M_w$ , NEIS- $M_S$ , NEIC-M, NEIS- $m_b$ , ISCJB- $m_b$ , ISCJB- $M_S$ , GFZ- $m_b$ , ISC- $m_b$ , ISC- $M_L$  (The National Earthquake Information Service (NEIS) is now the NEIC and is included only for old events). Our choice was to favour catalogue moment and surface-wave magnitudes, but we acknowledge that surface-wave magnitudes are not always accurate or directly comparable to moment magnitude for small events. The aftershocks with GCMT solutions (diamonds) have relative magnitudes that are slightly smaller (0.0–0.1 units) than the GCMT estimates but generally consistent. The exceptions are the aftershock on 2013 May 20 09:16:30, the GCMT estimate appears higher than our solution. Our main-shock moment is slightly high, but we do not account for source time-function differences in the computation. The two  $m_b$  catalogue magnitudes and the two outlying catalogue  $M_S$  magnitudes at  $\sim 3.75$  and 3.4 are the lower quality (Supporting Information Table S1). The most interesting result is the systematic difference between catalogue  $M_S$  and our  $M_w$ . The catalogue  $M_S$  bias persists even when both our inversion and the catalogue has a significant number of observations. Our observations are compatible with relationships between  $M_w$  and  $m_b$  and  $M_w$  and  $M_S$  estimated using global earthquake catalogues from Scordilis (2006), which are shown by the dashed lines in Fig. 6. A systematic discrepancy between  $M_S$  and  $M_w$  is expected for smaller-magnitude earthquakes, which generally have relatively short rise times and rupture durations (small slips and ruptures). The slope of 2/3 in our observations and Scordilis' (2006) empirical relationship agrees well with that expected from a simple ribbon fault model of

earthquake rupture (Haskell 1964; Kanamori & Anderson 1975). By definition,  $M_w$  is proportional to 2/3 the logarithm of the seismic moment. For small earthquakes, when the corner frequency is much higher than the frequency used to estimate the magnitude,  $M_S$  is proportional directly to the logarithm of the moment. The results show that although we have formally extended the relocation to include events with  $M_S$  as small as 2.9, we have only achieved an  $M_w$  threshold of about 4.

## DEPTH ESTIMATES

Penney *et al.* (2015) estimated the main shock and several aftershock centroid depths using teleseismic  $P$  and  $SH$  waveforms filtered with a long-period instrument response. Most of their well-matched signals were  $SH$  waveforms, which is not unusual for vertical strike-slip faulting. We performed a similar analysis using broad-band teleseismic displacement  $SH$  waveforms recorded in directions of  $SH$  radiation pattern extrema. We fit the observations using a simple half-space compatible with the model of Yamini-Fard *et al.* (2007), similar to the structure used by Penney *et al.* (2015). An example of  $SH$  data is shown in Fig. 7. We high-pass filter the waveforms with a corner period of 30 s, which retains some of the distinct features in the waveform (i.e. the  $sS$  depth phase) but removes long-period noise. We forward-modelled the observed waveforms by slightly adjusting faulting orientations, duration, moment and event depth. For the earth model, we assumed a Poisson solid in which the  $P$ -wave speed above the source was  $5.6 \text{ km s}^{-1}$  and the near-source density was  $2700 \text{ kg m}^{-3}$ . Mantle attenuation was included using  $P$ - and  $S$ -wave  $Q^*$ -values of 0.9 and 3.5, respectively. Our estimated main-shock centroid depth,  $\sim 6.0 \text{ km}$  is compatible with that estimated by Penney *et al.* (2015). Only six aftershocks provide usable  $S$ -wave signals (Fig. 7 and Supporting Information Fig. S5), and they were generally shallow ( $< 10 \text{ km}$ ). Our best estimates suggest that events on 05/12/2013, 05/18/2013 10:57:47 and 02/02/2014 locate between 6–8 km in depth; the events on 05/12/2013 are within

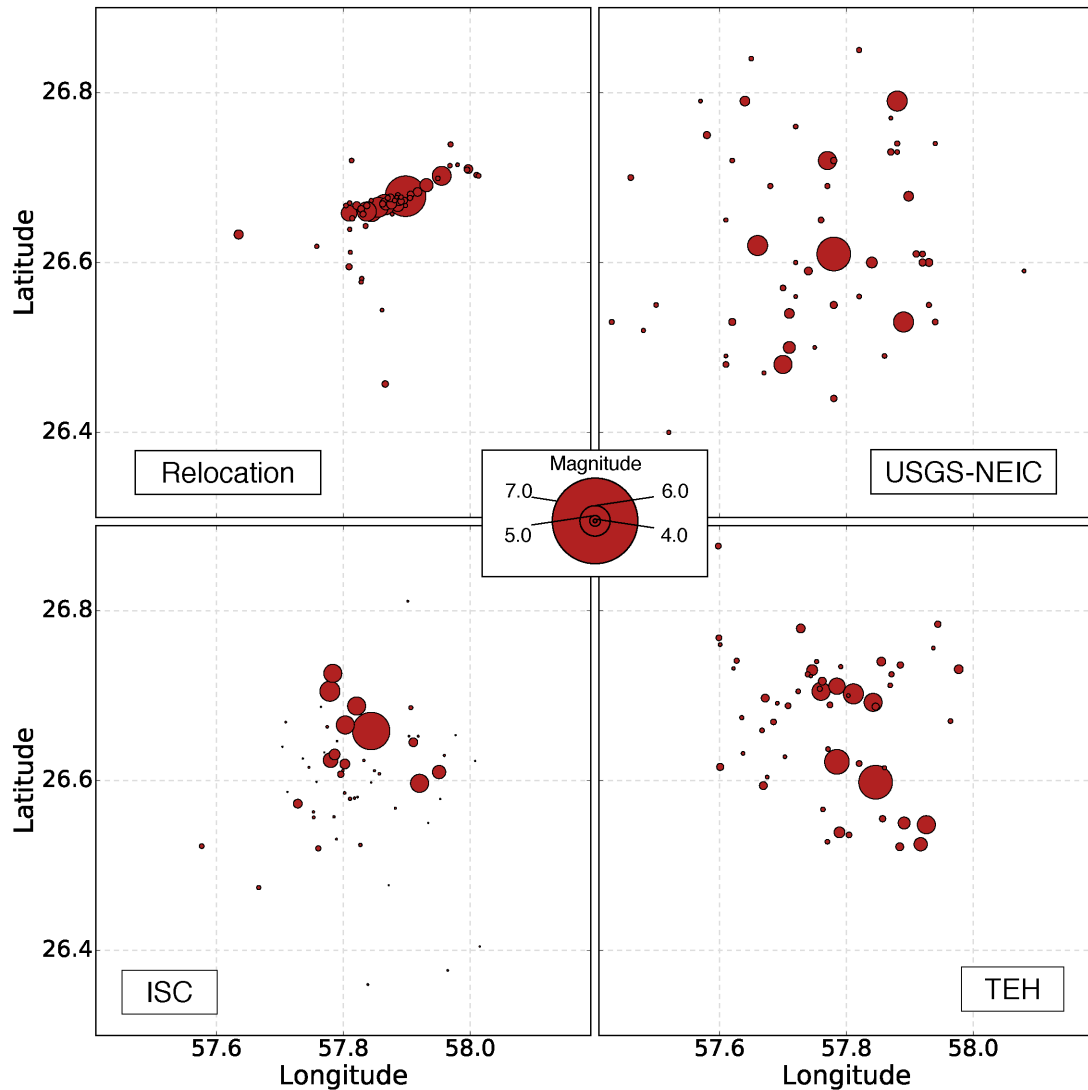


**Figure 5.** Comparison between our surface wave relocation results (quality-one and above from Supporting Information Table S1) and other teleseismic/regional earthquake catalogues. Top left panel shows the 54 relocated events from this study (scaled by their relative magnitude). Top right shows the US Geologic Survey (USGS-NEIC) locations, scaled by their respective magnitude—these are the initial locations for our inversion. Bottom left shows the International Seismological Centre (ISC) locations, scaled by the preferred magnitude specified above. The bottom right panel shows the Tehran University (TEH) locations, scaled by their respective magnitude.

$\sim 2$  km of estimates described in Penney *et al.* (2015). The aftershock that occurred on 05/18/2013 10:03:16 (Event 9 in Table 1) is notably shallower than other events in the sequence ( $\sim 5$  km). For that event, direct *SH* and *sSH* arrive close enough in time to not produce the split peaks that are observed for the other three aftershocks.

We attempted to estimate relative centroid depths using surface-wave amplitude spectra and spectral ratios. Rayleigh-wave surface wave spectra contain information about the depths of earthquakes (e.g. Tsai & Aki 1970). We computed spectral ratios for all the events with GCMT solutions in the sequence using seismograms at the closest available station, Kabul, Afghanistan (KBL,  $34.541^\circ\text{N}$ ,  $69.043^\circ\text{E}$ ,  $\Delta \sim 1390$  km, azimuth =  $48^\circ$ , inset in Fig. 1). Spectral amplitudes were estimated using frequency-dependent Gaussian windowing of the signal autocorrelation (Russel *et al.* 1988). We used several events as a reference spectra including the 2014 aftershock and the 2013-05-11 08:42 aftershock located close to the main-shock epicentroid. The spectral ratio results showed that

the three events to the east–northeast of the main-shock centroid differed from those west–southwest. Information on event depths was less clear—the patterns were not conclusive and differed when we investigated ratios at other stations at similar distances (ABKT, KMBO, DAMY, GNI, AATD).

Station KBL is located near a Rayleigh-wave radiation maximum and R1 GCMT-moment-normalized and cross-correlation-moment-normalized amplitude spectra are shown in Fig. 8 (plots of the corresponding seismograms are included in the Supporting Information Figs S1 and S2). We separated the early aftershocks, which locate to the east–northeast of the main shock from those to the west–southwest because they trend differently. Normalizing by the seismic moment places all events on the same relative amplitude scale but does not account for source time-function differences, which should only be significant for the main shock. The overall agreement in spectral amplitude at the longer periods (near 60 s) is very good considering that we have chosen only one of many stations used to estimate the moments. The main shock appears



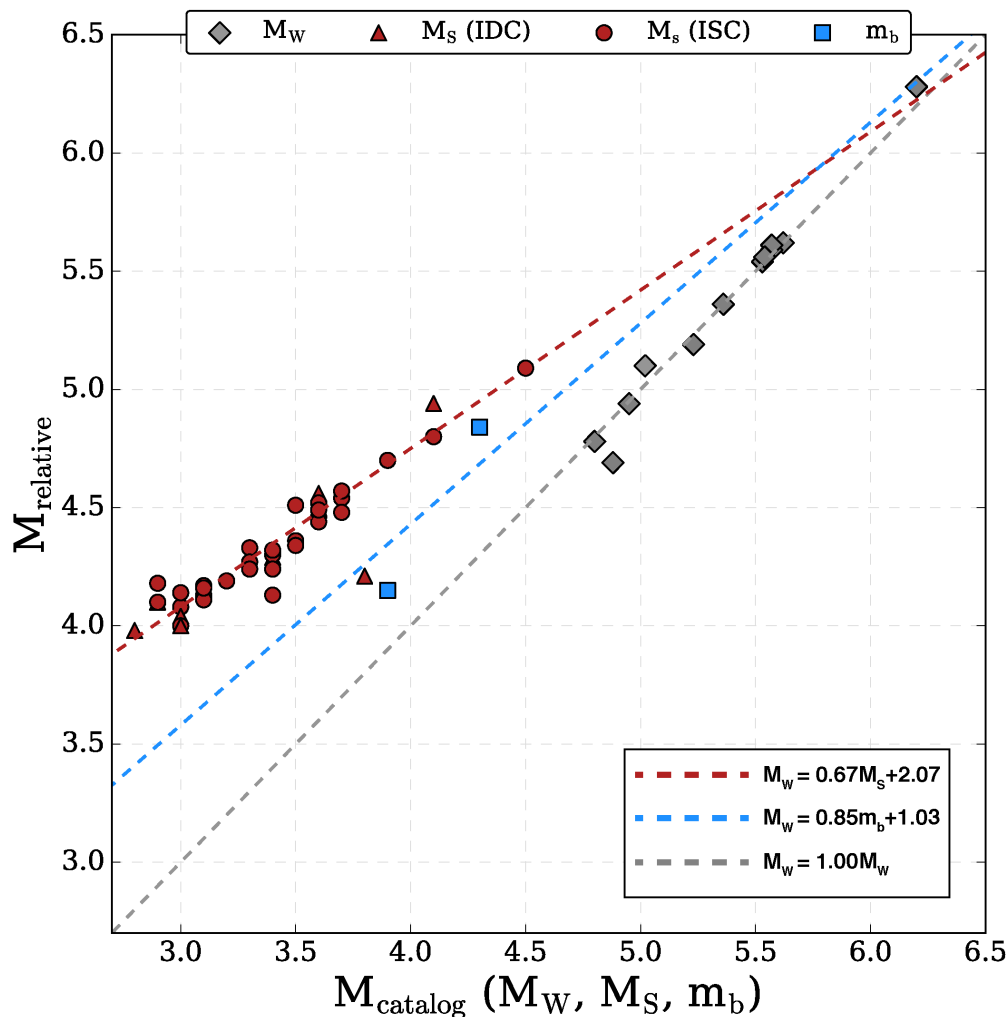


**Figure 6.** Relative magnitude results using surface wave cross-correlation observations (quality-one and above from Supporting Information Table S1). The figure shows the magnitude from the catalogue versus the relative moment magnitude. The shape and colour of the points correspond to the preferred magnitude type selected from the global catalogue. GCMT  $M_w$  is shown as light grey diamonds, ISC  $m_b$  is shown as light blue squares,  $M_s$  magnitudes from the ISC catalogues are shown in red circles while  $M_s$  magnitudes from the IDC catalogue are plotted as red triangles. The dashed lines show global empirical relations between each magnitude type and moment magnitude, specified in Scordilis (2006), coloured to match the magnitude type.

slightly enriched in long periods in the GCMT plot, this may be because we do not account for the source time function. The only significant difference in spectral amplitude is for the 2013-05-20 09:16 aftershock, which seems to have too large a GCMT moment (spectra are too low). Our estimate of the moment for this event is smaller, and using our value aligns the 60 s period amplitudes of that event closely to those of the other moderate-magnitude activity. The earthquake is one of the smaller GCMT catalogued events, so it may simply be a noisy set of observations (strangely, the catalogue  $M_w$  and seismic moment for this event are internally incompatible, suggesting the possibility of an erroneous entry or rounding). A difference in R1 radiation towards KBL is clear for the three early aftershocks located ENE of the main shock (Fig. 8). Events to the WSW all have a spectral amplitude minimum in the period range from 20–25 s. Using a simple velocity model using  $P$ -wave velocities from Yamini-Fard *et al.* (2007) and  $P/S$  ratio of 1.76, this notch would suggest a depth between 10–20 km, which we do not believe is accurate because of body wave results and InSAR observations (Penney *et al.* 2015) and inconsistency from station to station in our spectral ratios. The relative spectral amplitude at short-period (10–20 s) suggest that the ENE aftershocks are at a similar depth,

with event 03:09 perhaps locating slightly shallower. Of the foreshock and aftershocks WSW of the main shock, the short-period spectral amplitudes suggest that 00:06, 10:57, 10:54 and 08:42 events are shallower than events 02:08, 10:03, 14:26, 08:01 and 09:16. Love wave spectra are noisier and show broader spread at the longer periods, they also transmit less information on source depth.

## DISCUSSION

We relocated 54 earthquakes in the 2013–2014 Minab sequence located within southern Iran’s Makran accretionary wedge. The most striking result from this relocation is that the events align along strike on what appears to be one or two east/west left lateral structures. We also believe that the data suggest a model of the temporal evolution of the rupture. Fig. 3 illustrates this pattern, with the GCMT focal mechanisms coloured by time. The sequence started with an  $M_w$  5.1 foreshock (2013-05-09T08:01:34.900Z) located about 3 km to the west–southwest of the main-shock epicentroid. Immediately following the  $M_w$  6.2 main shock, the easternmost moderate-magnitude aftershock (2013-05-11T03:09:47.400Z),

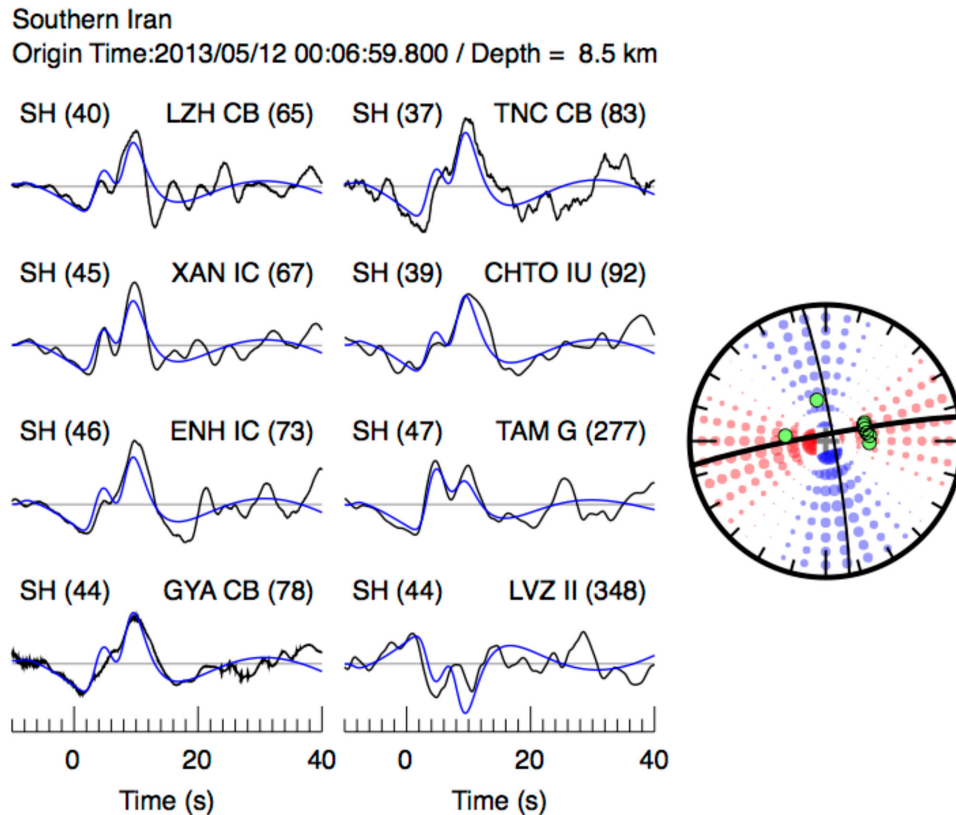


**Figure 7.** Forward modelling example of the aftershock that occurred on 2013 May 12 00:06:59. Black traces are the observed waveforms, blue traces are the predictions. The text above each waveform is the phase (*SH*), arc distance in degrees, station code, network code, and azimuth. The observed *SH* waveforms are high-pass filtered with a corner at 30 s, and cut  $-10$  and  $+40$  s around the predicted *SH* arrival time. Strike, dip and rake are estimated from the GCMT mechanism (s:82, d:86, r:27). The source–time function is set as a triangle, using the empirical duration derived from the GCMT (Ekström *et al.* 2012). Depth used to compute the predictions is 8.5 km. The focal sphere on the right shows the azimuthal coverage of the stations, the *SH* radiation amplitude, and the double couple fault planes. Additional body-wave modelling results are shown in Supporting Information Fig. S5.

located about 6–7 km east–northeast of the main shock. Over the next week, the moderate-magnitude activity migrated westward culminating with two moderate-magnitude events about 4–5 km west–southwest of the main shock on May 12 and two moderate magnitude events 5–7 km west–southwest of the main shock on May 18.

We speculate that the main shock ruptured east–northeastward from the vicinity of the foreshock to the easternmost moderate-magnitude aftershock, at a distance of about 10–15 km. A roughly 10 km length for the main shock remains consistent with other strike-slip faulting length relationships in table 2A of Wells & Coppersmith (1994). The distribution and shallow source depth of the seismicity in this sequence suggests that the main shock ruptured a 10 km long fault segment with a downdip width of about 8 km. Assuming a rupture area of roughly 80 km<sup>2</sup> and a shear modulus of 26 GPa, the corresponding mean slip is about one meter. The inferred stress drop would be slightly high but not unusual, between 3 and 10 MPa (Kanamori & Anderson 1975). The roughly 1 m average slip is comparable to average values that fit the InSAR observations (the uniform and distributed slip InSAR models from Penney *et al.* (2015) have an average slip of  $\sim 1.2$  m). The InSAR modelling included the aftershock induced deformation and a 20 km fault length, which introduces some uncertainty when positioning our relative event locations. The seismic moment of the InSAR model was roughly twice that of the GCMT main shock (Penney *et al.* 2015), or 25 per cent more than the combined GCMT moments of moderate-magnitude seismicity that occurred between the

satellite acquisition times (table 1). The discrepancy is modest, but opens the possibility for some post-seismic deformation. Fig. 9 is a Coulomb stress change (Toda *et al.* 2011) calculation using a 10 km long main shock with the GCMT faulting geometry and aligned with the InSAR model centroid. The centroid of the InSAR model may be biased west, because that analysis included deformation from the aftershocks. But our primary interest here is the relative positions of main-shock slip and the aftershocks. The stress changes are those expected on hypothetical, similarly oriented faults in the region and red indicates areas moved toward failure, blue indicates the opposite. Shown on top of the stress change pattern are the relocated aftershocks. The largest aftershocks locate within or near ( $\sim 2$  km) regions loaded by the main shock. Since the large aftershocks are adjacent to the fault edge, the Coulomb relationship is quite sensitive to the assumed main-shock fault position, length and faulting geometry. The location, timing and orientation of the events present a reasonable and consistent story for the sequence. Details of the model are limited by our knowledge of the main shock. For example, seismic and InSAR data provide little information on whether the main-shock rupture was unilateral or bilateral and thus other interpretations are feasible.

Penney *et al.* (2015) suggested that this sequence is similar to the 2013 September 24  $M_w$  7.7 Balochistan earthquake (e.g. Avouac *et al.* 2014; Barnhart *et al.* 2014; Jolivet *et al.* 2014; Zhou *et al.* 2015) on the eastern edge of the Makran accretionary structure. Both occurred in a region of maximum topography within the Makran accretionary wedge. This strike-slip deformation is thought to be

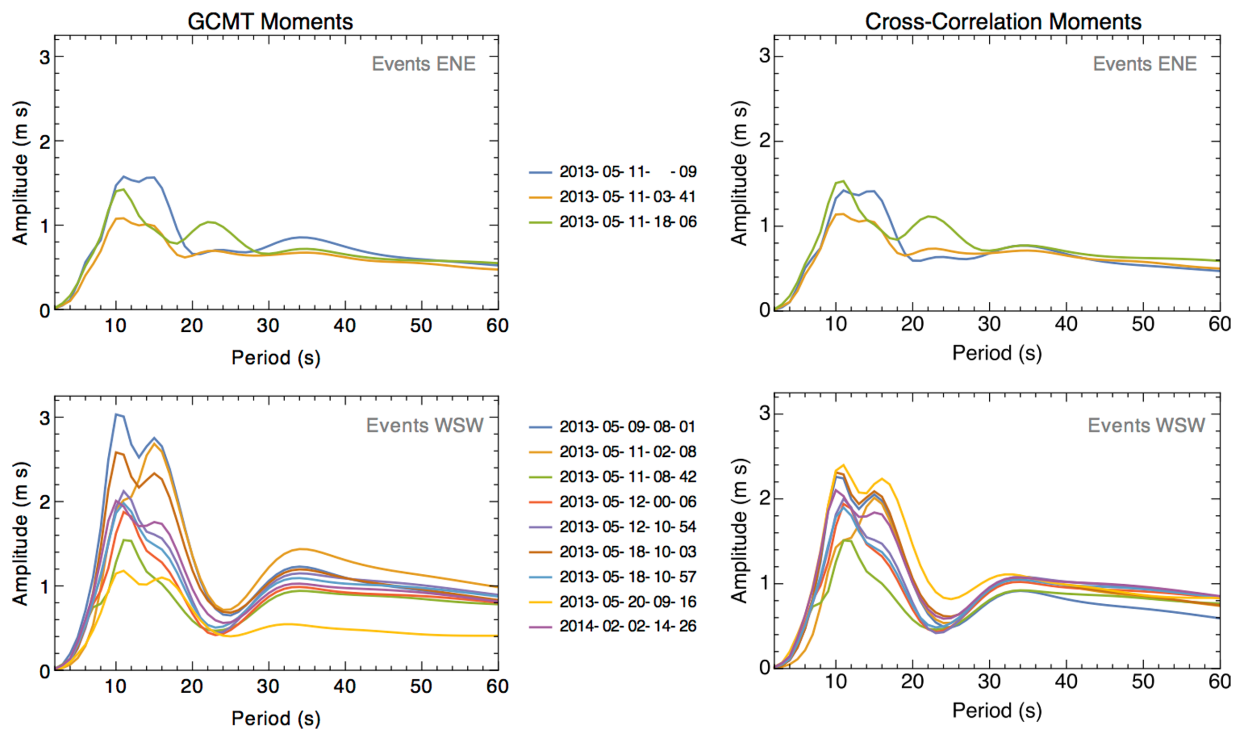


**Figure 8.** Left: Rayleigh-wave spectra for all GCMT catalogued earthquakes in the Minab sequence normalized by their respective GCMT moments and scaled by  $1.25 \times 10^{28}$  for display. Top-left panel shows immediate aftershocks, which locate east–northeast of the main-shock centroid. The bottom-left panel shows events that occurred later and are located west–southwest of the main-shock centroid. Right: spectra are normalized by their cross-correlation estimated moments and scaled by  $1.25 \times 10^{28}$  for display.

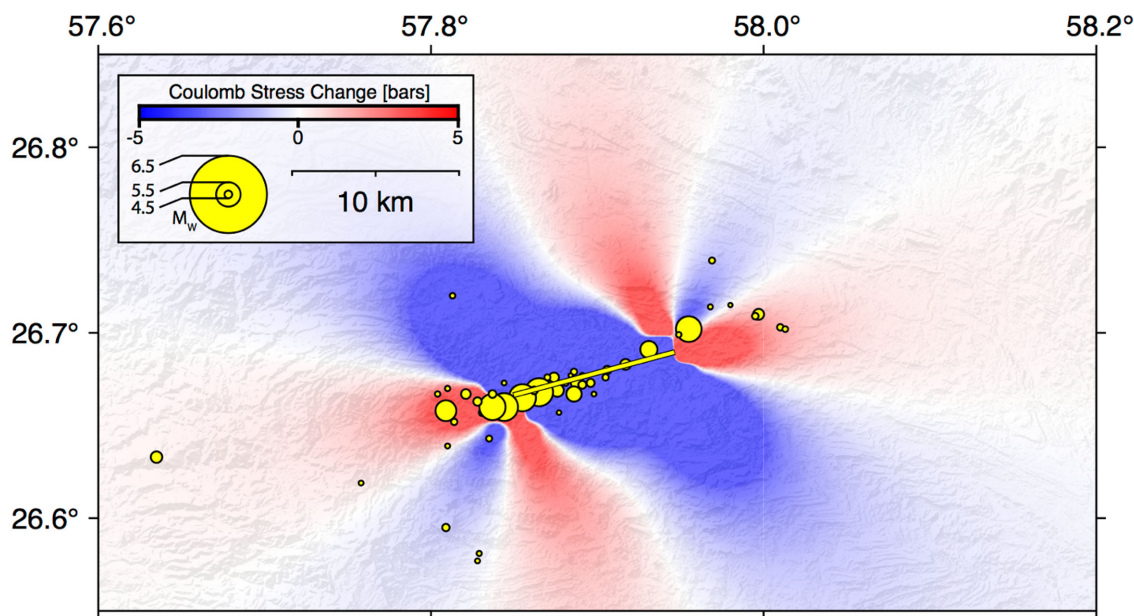


**Figure 9.** Static Coulomb stress change predictions for a model of the 2013 May 11  $M_w$  6.2, Minab main shock. The top of the rupture is at a depth of 1.5 km, the width is set at 8.0 km. The rupture length, 10 km, was estimated using the relationship in Wells & Coppersmith (1994) and equals the distance from the foreshock on 2013 May 9 and the eastern-most aftershock on 2013 May 11 03:09:47. The fault orientation is from the GCMT catalogue (strike: 255, dip: 88, rake:  $-16$ ). This model (shown as the yellow line) has its centroid fixed to the centroid of the uniform slip InSAR deformation model from Penney *et al.* (2015). The frictional coefficient was set to 0.60 and stress change is plotted at a depth of 6.0 km. The yellow circles are the relocated events.

driven by the combination of the regional plate motions and changes in gravitational potential as the mass of the accretionary wedge is redistributed (Penney *et al.* 2017). The left lateral faults that have been mapped in Makran are shown to be rather diffuse. Penney *et al.* (2015) describes a reasonable but more complex Minab-sequence

deformation associated with the stress field and multiple faults in part motivated by the lack of good aftershock locations. Our model of the sequence is simple given the dramatic improvement in event locations afforded by the surface-wave analysis. Indeed, the work is a demonstration of the power of large modern seismic data sets and

surface-wave cross-correlation derived relative locations to investigate even moderate-size earthquake sequences.

The Makran accretionary complex includes a substantial amount of accreted material along with the deformed southern margin of Eurasia. A likely choice for the boundary between the two is the transition from a relatively flat near-coastal plain and the uplifted southern margin of the Lut and Helmand blocks to the west and east respectively. Fig. 1 shows that the Minab region includes an area of relatively high elevation roughly twice as broad as the central Makran. Qualitatively the topography suggests that some additional uplift has occurred in the southwestern edge if the accretionary prism. The Minab earthquakes occur in between what might be called the Eurasian basement deformation and the elevated accreted material. The Minab sequence may thus be part of an accommodation between a small terrane caught along the western margin of the Arabian and Indian Ocean convergence with southern Eurasia. The left-lateral motion suggests transport of the small terrane towards the east, along the boundary between accreted material of the prism and the deformed backstop. The convergence between Arabia and Eurasia in this region is not aligned in the principal stress direction of the Minab earthquakes. Since no large east–west fault system exists in Western Makran, the Minab sequence may simply represent the release of the east–west component of strain associated with convergence and the uplift of the terrane.

The Minab earthquake is interesting and contributes to our understanding of tectonic strain accumulation and stress regimes in the Makran region (e.g. Zarifi *et al.* 2014; Walters *et al.* 2017). Perhaps what is most important in this investigation is the illustration of the power of surface-wave relocations to contribute to the analysis of moderate and strong earthquakes. We compared the surface-wave relocations with body-wave derived catalogued locations in Fig. 5. The improvement is dramatic, similar to the improvement of body-wave locations (e.g. Waldhauser & Ellsworth 2000) using cross-correlation methods, but applied over a relatively large fault system. In this case, relocation methods using teleseismic surface waves have highlighted tectonic features to a greater precision than catalogues using body wave arrivals at regional distances (TEH catalogue), as well as catalogues that include teleseismic observations to estimate locations (ISC and NEIC catalogues). Modern seismic data contain a wealth of information on precise relative locations, even when the closest station is more than a thousand kilometres in distance. The Minab sequence is unusual in that the aftershocks account for a large fraction of the main-shock moment. Future efforts to harvest this information leveraging the information in the GCMT catalogue could help increase in our understanding of regional tectonics and earthquake processes.

## CONCLUSIONS

We computed precise relative locations and magnitudes for 54 events in the 2013–2014 Minab earthquake sequence, Iran. *SH*-waveform modelling suggests event depths in the range from 8 km to as little as 4 km for the main shock and largest aftershocks. These precise relative relocations allow for a more in-depth interpretation of this earthquake sequence. The results suggest a relatively simple rupture on an east–west striking structure that included a relatively energetic aftershock sequence involved in the propagation of slip to the west in the week following the main shock. The analysis demonstrates the value of information contained in regional and teleseismic surface waves for the investigation of moderate-magnitude earthquakes in remote continental regions.

## ACKNOWLEDGEMENTS

This work was supported by the Air Force Research Laboratory under the Award FA9453-15-C-0064 and through partial support from the Defense Threat Reduction Agency under Award HDTRA1-11-1-0027. We thank the editor and two anonymous reviewers for comments that helped us improve this manuscript. We acknowledge the staff, support and data provided to the IRIS/USGS GSN, the Global Centroid-Moment-Tensor catalogue (Dziewonski *et al.* 1981; Ekström *et al.* 2012), International Seismological Centre (ISC), University of Tehran (TEH) and the United State Geologic Survey (USGS) Earthquake Hazards Program. The facilities of the IRIS Data Management System, and specifically the IRIS Data Management Center, were used for access to waveform and metadata required in this study. The IRIS DMS is funded through the National Science Foundation and specifically the GEO Directorate through the Instrumentation and Facilities Program of the National Science Foundation under Cooperative Agreement EAR-1063471. Thanks also to the developers of SAC (Goldstein *et al.* 2003), GMT (Wessel & Smith 1998), Coulomb (Toda *et al.* 2011), Python Software Foundation ([www.python.org](http://www.python.org)) and Obspy (Beyreuther *et al.* 2010; Megies *et al.* 2011; Krischer *et al.* 2015).

## REFERENCES

- Aster, R. & Thurber, C., 2013. *Parameter Estimation and Inverse Problems*, 2nd edn, Academic Press.
- Avouac, J. *et al.*, 2014. The 2013,  $M_w$  7.7 Balochistan earthquake, energetic strike-slip reactivation of a thrust fault, *Earth planet. Sci. Lett.*, **391**, 128–134.
- Barnhart, W., Hayes, G., Briggs, R., Gold, R. & Bilham, R., 2014. Ball-and-Socket tectonic rotation during the 2013  $M_w$  7.7 Balochistan earthquake, *Earth planet. Sci. Lett.*, **403**, 210–216.
- Beyreuther, M., Barsch, R., Krischer, L., Megies, T., Behr, Y. & Wassermann, J., 2010. ObsPy: a python toolbox for seismology, *Seismol. Res. Lett.*, **81**(3), 530–533.
- Byrne, D., Sykes, L. & Davis, D., 1992. Great thrust earthquakes and aseismic slip along the plate boundary of the Makran subduction zone, *J. geophys. Res.*, **97**(B1), 449–478.
- Cleveland, K.M. & Ammon, C.J., 2013. Precise relative earthquake location using surface waves, *J. geophys. Res.*, **118**(6), 2893–2904.
- Cleveland, K.M. & Ammon, C.J., 2015. Precise relative earthquake magnitudes from cross correlation, *Bull. seism. Soc. Am.*, **105**(3), 1792–1796.
- Cleveland, K.M., Vandemark, T. & Ammon, C.J., 2015. Precise relative locations for earthquakes in the northeast pacific region, *J. geophys. Res.*, **120**(10), 6960–6976.
- Dziewonski, A.M., Chou, T.A. & Woodhouse, J.H., 1981. Determination of earthquake source parameters from waveform data for studies of global and regional seismicity, *J. geophys. Res.*, **86**(B4), 2825–2852.
- Ekström, G., Nettles, M. & Dziewonski, A.M., 2012. The global CMT project 2004–2010: centroid-moment tensors for 13,017 earthquakes, *Phys. Earth planet. Inter.*, **200–201**, 1–9.
- Engdahl, E., Bergman, E., Myers, S.C. & Ryall, F., 2007. Improved ground truth in southern Asia using in-country data, analyst waveform review, and advance algorithms, in *29th Monitoring Research Review: Ground-Based Nuclear Explosion Monitoring Technologies*, doi:10.1017/CBO9781107415324.004.
- Frohling, E. & Szeliga, W., 2016. GPS constraints on interplate locking within the Makran subduction zone, *Geophys. J. Int.*, **205**(1), 67–76.
- Goldstein, P., Dodge, D., Firpo, M. & Minner, L., 2003. SAC2000: signal processing and analysis tools for seismologists and engineers, in *The IASPEI International Handbook of Earthquake and Engineering Seismology, Part B*, International Geophysics Series, Vol. 81, pp. 1613–1614, eds Lee, W.H.K., Kanamori, H., Jennings, P.C. & Kisslinger, C., Academic Press.

- Haskell, A.N., 1964. Total energy and energy spectral density of elastic wave radiation from propagating faults, *Bull. seism. Soc. Am.*, **54**(6), 1811–1841
- International Seismological Centre, 2014. ‘On-line bulletin, *Thatcham, United Kingdom*’. Available at: <http://www.isc.ac.uk>, last accessed June 2017.
- Jolivet, R. et al., 2014. The 2013  $M_w$  7.7 Balochistan earthquake: seismic potential of an accretionary wedge, *Bull. seism. Soc. Am.*, **104**(2), 1020–1030.
- Kanamori, H. & Anderson, D., 1975. Theoretical basis of some empirical relations in seismology, *Bull. seism. Soc. Am.*, **65**(5), 1073–1095.
- Krischer, L., Megie, T., Barsch, R., Beyreuther, M., Lecocq, T., Caudron, C. & Wassermann, J., 2015. ObsPy: a bridge for seismology into the scientific python ecosystem, *Comput. Sci. Disc.*, **8**(1), 14003, doi:10.1088/1749-4699/8/1/014003.
- Lohman, R.B. & Simons, M., 2005. Locations of selected small earthquakes in the Zagros mountains, *Geochem. Geophys. Geosyst.*, **6**(3), doi:10.1029/2004GC000849.
- Megies, T., Beyreuther, M., Barsch, R., Krischer, L. & Wassermann, J., 2011. ObsPy – What can it do for data centers and observatories?, *Ann. Geophys.*, **54**(1), 47–58.
- Menke, W., 2012. *Geophysical Data Analysis: Discrete Inverse Theory*, 3rd edn, Academic Press.
- Penney, C., Copley, A. & Oveisi, B., 2015. Subduction tractions and vertical axis rotations in the Zagros–Makran transition zone, SE Iran: the 2013 May 11  $M_w$  6.1 Minab earthquake, *Geophys. J. Int.*, **202**(2), 1122–1136.
- Penney, C. et al., 2017. Megathrust and accretionary wedge properties and behaviour in the Makran subduction zone, *Geophys. J. Int.*, **209**(3), 1800–1830.
- Russel, D., Herrmann, R. & Hwang, H., 1988. Application to frequency variable filters to surface wave amplitude analysis, *Bull. seism. Soc. Am.*, **78**(1), 339–354.
- Samsonov, S.V. & Czarnogorska, M., 2013. Ground deformation produced by 2013  $M_6.1$  Minab earthquake in Iran mapped with RADARSAT-2 InSAR, *Geological Survey of Canada, Open File*, **7528**, doi:10.4095/293320.
- Schaff, D.P. & Richards, P.G., 2011. On finding and using repeating seismic events in and near China, *J. geophys. Res.*, **116**(B3), 1–20.
- Schaff, D.P. & Richards, P.G., 2014. Improvements in magnitude precision, using the statistics of relative amplitudes measured by cross correlation, *Geophys. J. Int.*, **197**(1), 335–350.
- Scordilis, E.M., 2006. Empirical global relations converting  $M_S$  and  $m_b$  to moment magnitude, *J. Seismol.*, **10**(2), 225–236.
- Smith, G., McNeill, L., Henstock, T.J. & Bull, J., 2012. The structure and fault activity of the Makran accretionary prism, *J. geophys. Res.*, **117**(B07407), 1–17.
- Tehran University, Institute of Geophysics, 2016. ‘University of Tehran, 16 Azar Street, Enghelab Ave., Tehran, Iran’. Available at: <http://irsc.ut.ac.ir/>, last accessed June 2017.
- Toda, S., Stein, R.S., Sevilgen, V. & Lin, J., 2011. Coulomb 3.3 Graphic-Rich deformation and Stress-Change software for earthquake, tectonic, and volcano research and Teaching—user guide, *U.S. Geological Survey, Open-File Report 2011-1060*, 63.
- Tsai, Y. & Aki, K., 1970. Precise focal depth determination from amplitude spectra of surface waves, *J. geophys. Res.*, **75**(29), 5729–5744.
- Vernant, P. et al., 2004. Present-day crustal deformation and plate kinematics in the Middle East constrained by GPS measurements in Iran and Northern Oman, *Geophys. J. Int.*, **157**(1), 381–398.
- Waldhauser, F. & Ellsworth, W.L., 2000. A double-difference earthquake location algorithm: method and application to the Northern Hayward Fault, California, *Bull. seism. Soc. Am.*, **90**(6), 1353–1368.
- Walters, R.J., England, P.C. & Houseman, G.A., 2017. Constraints from GPS measurements on the dynamics of the zone of convergence between Arabia and Eurasia, *J. geophys. Res.*, **122**(2), 1470–1495.
- Wells, D.L. & Coppersmith, K.J., 1994. New empirical relationships among magnitude, rupture length, rupture width, rupture area, and surface displacement, *Bull. seism. Soc. Am.*, **84**(4), 974–1002.
- Wessel, P. & Smith, W.H.F., 1998. New, improved version of generic mapping tools released, *EOS, Trans. Am. geophys. Un.*, **79**(47), 579.
- Weston, J., A.M.G.F. & Funning, G.J., 2011. Global compilation of interferometric synthetic aperture radar earthquake source models: 1. Comparisons with seismic catalogs, *J. geophys. Res.*, **116**(B8), 1–20.
- Yamini-Fard, F. & Hatzfeld, D., 2008. Seismic structure beneath Zagros–Makran transition zone (Iran) from teleseismic study: seismological evidence for underthrusting and buckling of the Arabian plate beneath central Iran, *J. Seismol. Earthq. Eng.*, **10**(1), 11–24.
- Yamini-Fard, F., Hatzfeld, D., Farahbod, A.M., Paul, A. & Mokhtari, M., 2007. The diffuse transition between the Zagros continental collision and the Makran oceanic subduction (Iran): microearthquake seismicity and crustal structure, *Geophys. J. Int.*, **170**(1), 182–194.
- Zarifi, Z., Nilfouroushan, F. & Raeesi, M., 2014. Crustal stress map of Iran: Insight from seismic and geodetic computations, *Pure appl. Geophys.*, **171**, 1219–1236.
- Zhou, Y., Elliott, J.R., Parsons, B. & Walker, R.T., 2013. The 2013 Balochistan Earthquake: An Extraordinary or Completely Ordinary Event?, *Geophys. Res. Lett.*, **42** (2015): 6236–6243.

## SUPPORTING INFORMATION

Supplementary data are available at *GJI* online.

**Figure S1.** Rayleigh-wave signals from the larger events in the Minab sequence observed at station KBL, Kabul, Afghanistan. Each signal is normalized for plotting, the time reference is the event origin, and the top axis shows group speed in  $\text{km s}^{-1}$ . The signals show a strong similarity, but subtle variations are notable, such as the slightly lower-frequency main shock (second from top) and subtle changes in the relative amplitudes of the long- and short-period surface waves.

**Figure S2.** Love-wave signals from the larger events in the Minab sequence observed at station KBL, Kabul, Afghanistan. Each signal is normalized for plotting, the time reference is the event origin, and the top axis shows group speed in  $\text{km s}^{-1}$ . The signals show a strong similarity, but subtle variations are notable, such as the slightly lower-frequency main shock (second from top) and the variation in relative amplitudes of the long- and short-period signals.

**Figure S3.** Original (left) and final (right) *SH* wave arrival times at Tamanrasset, Algeria (TAM, 22.79° N, 5.53° E). TAM is located near an *SH* radiation pattern maxima for these events. Each panel corresponds to one event in the sequence (left panel is labelled with the origin time, right panel is labelled with event index). Waveforms are high-pass filtered at 80 s, arrival times were computed through iasp91 velocity model. We only show the events with a clear *SH* arrival. The surface-wave relocation improves the alignment of the teleseismic *S* waves observed by several seconds.

**Figure S4.** Statistical summary of the relocation results (quality-one and above from Supporting Information Table S1). Panel (a) shows the original and final observed–predicted traveltimes residuals. Panel (b1) shows the origin time-shifts, outliers at  $-7$  and  $15$  are the two low-quality events set to one in Supporting Information Table S1 (discussed in the results). Panel (b2) shows the absolute origin time-shifts. Panel (c) shows how much each event shifted during the relocation.

**Figure S5.** Additional body-wave forward modelling solutions for the main shock and five additional aftershocks in the Minab sequence. Black traces are the observed waveforms, blue traces are the predictions. The text above each waveform is the phase (*SH*), arc distance in degrees, station code, network code, and azimuth. The observed *SH* waveforms are high-pass filtered with a corner at 30 s, and cut  $-10$  and  $+40$  s around the predicted *SH* arrival time.

Strike, dip and rake are estimated from the GCMT mechanism. The source–time function is set as a triangle, using the empirical duration derived from the GCMT (Ekström *et al.* 2012). Earth-model parameters for the analyses are  $t^*$  ( $t^* - P = 0.9$ ,  $t^* - S = 3.5$ ),  $P$ -wave speed above the source ( $5.6 \text{ km s}^{-1}$ ,  $V_p/V_s = \text{Sqrt}[3]$ ), and density ( $2.7 \text{ g cm}^{-3}$ ). The focal sphere on the right shows the azimuthal coverage of the stations, the  $SH$  radiation amplitude and the double couple fault planes.

**Figure S6.** Magnitude versus time of earthquakes in the Minab region (26–27.5N, 57–58.5E) from the ISC bulletin. Magnitudes are selected on the criteria described in the Relative Earthquake Magnitudes section.

**Table S1.** Results from this study, date and time are the NEIC origin times. Origin time-shift is the change from the NEIC origin time to the centroid time of the event. The latitude and longitude are the coordinates for the final and original locations.  $std\_la/lo$  are the 1-sigma standard deviation location uncertainties (in kilometres) in latitude and longitude direction for each event. The  $M_w$

values are the computed relative moment magnitudes. *Catmag* are the preferred global earthquake catalogue magnitudes, *catMagType* is the magnitude type in these catalogues, *catMagSource* is the catalogue name, *catMagObs* is the number of observations used to compute the catalogue magnitude, *NCCobs* is the number of unique normalized cross-correlation observations above 0.80 used for calculating locations and magnitudes. *Quality* is defined as the following: quality-zero is poor with no consistent observations, quality-one are events that only link with the low link criteria of 4, and quality-two events are the best solutions with a conservative linking criteria (12) specified in Cleveland & Ammon (2013).

Please note: Oxford University Press is not responsible for the content or functionality of any supporting materials supplied by the authors. Any queries (other than missing material) should be directed to the corresponding author for the paper.